

Tangential Fluid flow within 3D narrow fissures: Conservative velocity fields on associated triangulations and transport processes.

Fernando A Morales^a, Jorge M Ramírez^a

^a*Escuela de Matemáticas Universidad Nacional de Colombia, Sede Medellín
Calle 59 A No 63-20 - Bloque 43, of 106, Medellín - Colombia*

Abstract

For a fissured medium with uncertainty in the knowledge of fractures' geometry, a conservative tangential flow field is constructed, which is consistent with the physics of stationary fluid flow in porous media and an interpolated geometry of the cracks. The flow field permits computing preferential fluid flow directions of the medium, rates of mechanical energy dissipations and a stochastic matrix modeling stream lines and fluid mass transportation, for the analysis of solute/contaminant mass advection-diffusion as well as drainage times.

Keywords: fissured media, preferential flow, probabilistic modeling
2010 MSC: 76S05, 97M99, 94A17

1. Introduction

Fissured media are common geological structures. In such a medium, fast flow occurs on the cracks while the rock matrix constitutes the slow flow region. The associated transport phenomenon has been extensively studied from several points of view and at different scales of modeling due to its remarkable importance in different fields such as: oil extraction, water supply, pollution of subsurface streams and soils, waste management, etc. Several models of coupled systems of partial differential equations have been proposed, such as double [2, 4] and multiple porosity systems [22], microstructure models [19] and the coupling of laws at different scales: see [3] for an analytic approach of a Darcy-Stokes system and see [13] for a numerical treatment of a Darcy-Brinkman system. In addition, various numerical [1, 15] or numerical/analytical [18, 24] works have dealt with the discretization and numerical aspects of the proposed models.

For small values of the Reynolds number, the saturated flow within the fissures is predominantly parallel to the surface hosting it. This fact has been mathematically shown in [2, 20] using homogenization techniques and in [10, 16, 17] via asymptotic analysis. Assuming further that fissures are thin enough as to forgo any transverse variation of velocities, and that the surrounding rock matrix is impermeable, two degrees of freedom at each point remain to be resolved for a complete identification of the velocity field. Another important aspect is that surveys of fissured media at the field scale are usually performed at discrete (albeit numerous) sampling points (see [23] for an imaging method). The three-dimensional geometry of the fissure is then usually modeled as a triangulated surface with nodes located on points of known coordinates. For physical processes that depend on the fissure's geometry like fluid flow, it is therefore desirable to construct models that yield approximate solutions at the resolution of the triangulated surface.

The considerations laid out in the previous paragraph encompass the main motivation for the present work. Our starting point is the Darcy's equation for the two-dimensional flow velocity and pressure on the region of the X-Y plane limited by the fissure. This approach is hence limited to fissures whose three-dimensional triangulated

^{*}This material is based upon work supported by the project HERMES 27798 from Universidad Nacional de Colombia, Sede Medellín.

^{*}Corresponding Author

Email address: famoralesj@una1.edu.co (Fernando A Morales)

surface can be orthogonally projected onto a triangulated region of the X-Y plane in a biunivoque way. The flow is driven by the gravitational potential and a prescribed external pressure potential along the domain. We then compute a conservative two-dimensional velocity field that is piece-wise constant on the triangulation elements, and that best approximates the solution to the discretized Darcy's equation. By conservative in this context, we mean a velocity field for which the net discharge along each element boundary vanishes. The final step in the construction is a lifting operation, again conservative, yielding the corresponding three-dimensional velocity field everywhere parallel to the triangulated surface.

The main feature of the proposed model is its simplicity. Through the action of linear operators whose dimension is comparable to the number of elements in the triangulation, our methodology yields approximate streamlines which are parallel among them within each triangle, and everywhere parallel to the triangulated surface.

We present two applications of the proposed model aimed at quantifying the fissure's geometry effect on flow and transport. First we consider the problem of dispersion of a tracer that is being advected within the fissure by the constructed velocity field. The evolution of the concentration of the tracer can be characterized in discrete time by a linear operator which is explicitly derived here. As a second application, we consider different mechanisms of energy dissipation. Functionals to estimate dissipation rates associated to curvature, friction and gravity are explicitly derived and computed for fissures of different exemplifying geometries.

We close this section introducing the notation. Vectors in \mathbb{R}^3 are denoted with bold characters $\mathbf{x} = (x_1, x_2, x_3) \in \mathbb{R}^3$, $|\mathbf{x}|$ indicates the Euclidean norm of \mathbf{x} , \mathbf{x}^T its transpose, and $\tilde{\mathbf{x}} = (x_1, x_2)$ its projection on the first two coordinates. Projections along vectors or onto subspaces are denoted by the operator Proj, for instance, if $\mathbf{u} \in \mathbb{R}^d$,

$$\text{Proj}_{\mathbf{x}}(\mathbf{u}) \stackrel{\text{def}}{=} (\mathbf{u} \cdot \mathbf{x}) \frac{\mathbf{x}}{\|\mathbf{x}\|^2} \quad (1)$$

denotes the projection of \mathbf{u} along the direction of \mathbf{x} . For a given subset A of \mathbb{R}^d , $d = 1, 2, 3$, we denote its Lebesgue measure by $|A|$, its cardinal by $\#A$, its closure by $\text{cl}(A)$ and its boundary by ∂A . The symbol $\mathbb{1}_A$ denotes the indicator function of the set A : $\mathbb{1}_A(\mathbf{x}) = 1$ if $\mathbf{x} \in A$, zero otherwise.

2. The triangulated fissure and the class of element-wise constant vector fields

Our approach rests on the assumption that the fissure's physical surface can be approximated by a piecewise linear affine triangulation constructed from discrete sampled points. Below, we start delimiting the type of fissures to be analyzed.

Definition 1. Let $S = \{\tilde{\mathbf{x}}_1, \tilde{\mathbf{x}}_2, \dots, \tilde{\mathbf{x}}_n\}$ be the set of distinct points in \mathbb{R}^2 , such that for all $i = 1, \dots, n$, the three-dimensional location $(\tilde{\mathbf{x}}_i, \zeta(\tilde{\mathbf{x}}_i))$ of the fissure surface is known; S will be called the **sample set**. The **sample domain** $\Omega \subset \mathbb{R}^2$ is the convex hull of S .

Hypothesis 1. We assume that the **fissure** is a surface $\Gamma = \{(\tilde{\mathbf{x}}, \zeta(\tilde{\mathbf{x}})) : \tilde{\mathbf{x}} \in G\}$ defined by a continuous function $\zeta : G \rightarrow \mathbb{R}$ on a convex domain G of \mathbb{R}^2 with $\Omega \subseteq G$. In particular the continuous 2-D manifold Γ has an Atlas containing one element.

The sample domain $\Omega \subset \mathbb{R}^2$ will be partitioned with a **triangulation** \mathcal{T} constructed as follows. See Figure 1.

Definition 2. The **triangular mesh** \mathcal{T} is a collection of open triangular disjoint subsets of Ω such that if any two triangles $K, L \in \mathcal{T}$ satisfy $|\partial K \cap \partial L| > 0$ then, $\partial K \cap \partial L$ is a common edge. We also introduce the following notation associated to the triangulation \mathcal{T} :

- (i) Denote by \mathcal{E} the **edges** of the triangulation; $\mathcal{E}_{\text{bdry}}$ are the edges of the triangulation contained in the boundary $\partial\Omega$ of the domain and the edges $\mathcal{E}_{\text{itfc}} \stackrel{\text{def}}{=} \mathcal{E} - \mathcal{E}_{\text{bdry}}$ are the interfaces between pairs of elements in \mathcal{T} .
- (ii) Edges in $\mathcal{E}_{\text{bdry}}$ are regarded as "boundary elements" of an extended triangulation $\mathcal{T}_{\text{ext}} \stackrel{\text{def}}{=} \mathcal{T} \cup \mathcal{E}_{\text{bdry}}$.

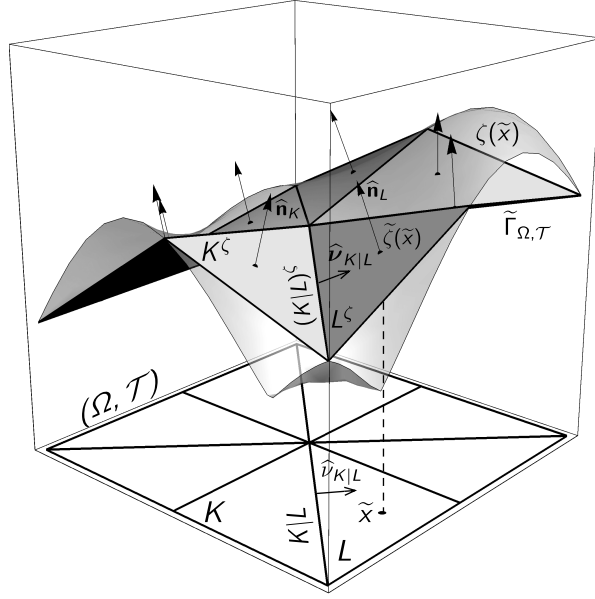


Figure 1: Schematic representation of a fissure, a triangulation and its associated elements described in Definitions 2 and 3

- (iii) Any edge $e \in \mathcal{E}$ is common to two elements, namely $K \in \mathcal{T}, L \in \mathcal{T}_{\text{ext}}$ and it is thus denoted as $e = K|L = L|K$. Its length is $\sigma_e \stackrel{\text{def}}{=} |e|$.
- (iv) Given an element $K \in \mathcal{T}$ and one of its edges $e = K|L, L \in \mathcal{T}_{\text{ext}}$, we denote by $\hat{\nu}_{K|L}$ the unitary vector that is normal to e and points outwards K . See Figure 1.

In particular, the numerical experiments in Section 5.3, will assume that \mathcal{T} is a Delaunay triangulation of the sample set S . We now introduce the notation for the associated three-dimensional triangular elements.

Definition 3. Let Ω, \mathcal{T} be as in Definitions 1 and 2,

- (i) Let $K \subseteq \Omega \subset \mathbb{R}^2$ be a triangular element of \mathcal{T} with vertices $\{z_\ell : 1 \leq \ell \leq 3\}$. We define the K^ζ as the triangle formed by the points $\{(z_\ell, \zeta(z_\ell)) : 1 \leq \ell \leq 3\} \subset \mathbb{R}^3$.
- (ii) For any point $\tilde{x} \in \text{cl}(K)$, we define $\tilde{\zeta}(\tilde{x})$ as the unique point \mathbf{x} in K^ζ such that its horizontal projection agrees with \tilde{x} , namely $\mathbf{x} - (\mathbf{x} \cdot \hat{\mathbf{k}})\hat{\mathbf{k}} = \tilde{x}$. In particular, the function $\tilde{\zeta}$ agrees with ζ on the sample set S .
- (iii) For an edge $e \in \mathcal{E}$ we define e^ζ in the analogous way and denote its length by σ_e^ζ .
- (iv) The *triangulation* of Γ relative to Ω and \mathcal{T} , is given by the collection of the previously defined triangles; it is denoted by

$$\tilde{\Gamma}_{\Omega, \mathcal{T}} \stackrel{\text{def}}{=} \bigcup \{K^\zeta : K \in \mathcal{T}\}. \quad (2)$$

- (v) The vector $\hat{\mathbf{n}}_K$ indicates the upwards unitary vector, normal to the surface of the element K^ζ .
- (vi) For each $K \in \mathcal{T}, L \in \mathcal{T}_{\text{ext}}$, $\hat{\nu}_{K|L}$ denotes the vector that is normal to both $\hat{\mathbf{n}}_K$ and the edge $(K|L)^\zeta$, pointing outwards K^ζ .

We will throughly use vector fields of two distinct types: fields defined over the sample domain Ω and with values on \mathbb{R}^2 ; the others defined over the triangulated surface $\tilde{\Gamma}_{\Omega, \mathcal{T}}$ and with values on \mathbb{R}^3 . Moreover, we will specialize

on those vector fields that are constant over the triangles that compose their corresponding domains of definition. The space of **element wise constant** flow fields on Ω is denoted by

$$\mathbf{H}(\Omega, \mathcal{T}) \stackrel{\text{def}}{=} \left\{ \mathbf{v}(\tilde{\mathbf{x}}) = \sum_{K \in \mathcal{T}} \mathbf{v}_K \mathbb{1}_K(\tilde{\mathbf{x}}) : \mathbf{v}_K \in \mathbb{R}^2, \text{ for all } K \in \mathcal{T} \right\}, \quad (3)$$

and in particular, a vector field in $\mathbf{H}(\Omega, \mathcal{T})$ will be called **conservative** if it belongs to the space $\mathbf{V}(\Omega, \mathcal{T})$ defined as follows,

$$\mathbf{V}(\Omega, \mathcal{T}) \stackrel{\text{def}}{=} \left\{ \mathbf{v} \in \mathbf{H}(\Omega, \mathcal{T}) \text{ such that if } |\partial K \cap \partial L| > 0, \text{ then } \mathbf{v}_K \cdot \hat{\nu}_{K|L} = -\mathbf{v}_L \cdot \hat{\nu}_{L|K} \right\}. \quad (4)$$

Observe that $\mathbf{V}(\Omega, \mathcal{T})$ is a special case of the Raviart-Thomas finite element space (see [9]). We also define the space of **conservative potentials** $E(\Omega, \mathcal{T})$ by

$$E(\Omega, \mathcal{T}) \stackrel{\text{def}}{=} \left\{ q \in P_1(\Omega, \mathcal{T}) : \mathbf{grad} q \in \mathbf{V}(\Omega, \mathcal{T}) \right\}. \quad (5)$$

Equivalently, if $\mathbf{grad} : P_1(\Omega, \mathcal{T}) \rightarrow \mathbf{H}(\Omega, \mathcal{T})$, then $E(\Omega, \mathcal{T}) \equiv \mathbf{grad}^{-1}(\mathbf{V}(\Omega, \mathcal{T}))$.

Among three-dimensional vector fields defined on the triangulated surface $\tilde{\Gamma}_{\Omega, \mathcal{T}}$, we will be interested on element-wise constant vector fields that are everywhere parallel to the surface. We introduce the space

$$\tilde{\mathbf{H}}(\Omega, \mathcal{T}) \stackrel{\text{def}}{=} \left\{ \mathbf{w}(\mathbf{x}) = \sum_{K \in \mathcal{T}} \mathbf{w}_K \mathbb{1}_K(\mathbf{x}) : \mathbf{w}_K \in \mathbb{R}^3, \mathbf{w}_K \cdot \hat{\mathbf{n}}(K) = 0 \text{ for all } K \in \mathcal{T}, \mathbf{x} \in \Omega \right\}, \quad (6)$$

as well as the corresponding space of conservative vector fields

$$\tilde{\mathbf{V}}(\Omega, \mathcal{T}) \stackrel{\text{def}}{=} \left\{ \mathbf{w} \in \tilde{\mathbf{H}}(\Omega, \mathcal{T}) \text{ such that if } |\partial K \cap \partial L| > 0, \text{ then } \mathbf{w}_K \cdot \hat{\nu}_{K|L} = -\mathbf{w}_L \cdot \hat{\nu}_{L|K} \right\}. \quad (7)$$

3. Construction of the velocity field

In this section we construct a family of conservative velocity fields hosted on the triangulated surface $\tilde{\Gamma}_{\Omega, \mathcal{T}}$ and defined by the surface's geometry as well as the pressure potential. This is accomplished in two steps. First, a two-dimensional **master conservative vector field** $\mathbf{v} \in \mathbf{V}(\Omega, \mathcal{T})$ is calculated from the equations of fluid flow in porous media. Second, the vector field is lifted to the surface $\tilde{\Gamma}_{\Omega, \mathcal{T}}$ in such a way that the resulting **global velocity field** \mathbf{u} lands in the space $\tilde{\mathbf{V}}(\Omega, \mathcal{T})$.

Our starting point is the saturated porous media flow equation on Ω :

$$a \mathbf{v} + \mathbf{grad} p = -g \rho \mathbf{grad} \zeta - \mathbf{grad} P, \quad (8a)$$

$$\mathbf{div} \mathbf{v} = 0, \quad \text{in } \Omega. \quad (8b)$$

$$p = 0, \quad \text{on } \partial\Omega. \quad (8c)$$

Here, a is the **flow resistance** (the fluid viscosity times the inverse of the medium permeability tensor), P is the external pressure potential, g is the gravity, ρ is the fluid density and ζ is the function defining the fissure in Definition 1. The Problem (8) above is composed by the Darcy constitutive equation (8a), the mass conservation equation (8b) and the drained (Dirichlet) boundary conditions (8c). The external pressure gradient $\mathbf{grad} P$ and the geometric gradient $\mathbf{grad} \zeta$ are incorporated as driving forces in Equation (8a). Finally, Equation (8b) states that the system is free of sources and therefore conservative.

It is a well-known fact that the System (8) is well-posed (see [12, 9]) in the continuous case, consequently it can be solved in a discrete setting associated to a sampling triangulation \mathcal{T} using numerical analysis methods e.g., mixed finite element methods (see, [12]). In order to attain the numerical solution of Equation (8) consistent

with the requirement $\mathbf{v} \in \mathbf{V}(\Omega, \mathcal{T})$, we must define the spaces to which the numerical approximations of p , P and ζ must belong. The **linear space** associated to Ω, \mathcal{T} is defined as

$$P_1(\Omega, \mathcal{T}) \stackrel{\text{def}}{=} \left\{ q = \sum_{K \in \mathcal{T}} q_K \mathbb{1}_K : q \text{ continuous and } q_K \in P_1(K), \text{ for all } K \in \mathcal{T} \right\}, \quad (9)$$

where

$$P_1(K) \stackrel{\text{def}}{=} \{ ax + by + c : a, b, c \in \mathbb{R} \}. \quad (10)$$

Clearly, the approximated surface $\tilde{\zeta}$ belongs to $P_1(\Omega, \mathcal{T})$. Moreover, if $q \in P_1(\Omega, \mathcal{T})$, then $\mathbf{grad} q \in \mathbf{H}(\Omega, \mathcal{T})$.

3.1. Construction of the master conservative velocity field \mathbf{v}

Let $P \in P_1(\Omega, \mathcal{T})$ be given. The construction of the master conservative flow field $\mathbf{v} \in \mathbf{V}(\Omega, \mathcal{T})$ is accomplished in three steps. First, compute (see [8, 9, 14]) the unique numerical solution $p_0 \in P_1(\Omega, \mathcal{T})$ to

$$-\mathbf{div}(\mathbf{grad} p) = \rho g \mathbf{div} \mathbf{grad} \tilde{\zeta} + \mathbf{div} \mathbf{grad} P \quad \text{in } \Omega, \quad (11)$$

$$p = 0 \quad \text{on } \partial\Omega. \quad (12)$$

Next, compute the **primary velocity field** $\mathbf{v}_0 \in \mathbf{H}(\Omega, \mathcal{T})$ associated to Γ as

$$\mathbf{v}_0 \stackrel{\text{def}}{=} -\frac{1}{a} \sum_{K \in \mathcal{T}} (\mathbf{grad} p_0 + \mathbf{grad} P + \rho g \mathbf{grad} \tilde{\zeta}) \mathbb{1}_K. \quad (13)$$

Finally, in order to guarantee conservation of mass, define the **master conservative velocity field** $\mathbf{v} \in \mathbf{V}(\Omega, \mathcal{T})$ as

$$\mathbf{v} \stackrel{\text{def}}{=} \text{Orthogonal Projection of the primary velocity field } \mathbf{v}_0 \in \mathbf{H}(\Omega, \mathcal{T}) \text{ onto the space } \mathbf{V}(\Omega, \mathcal{T}). \quad (14)$$

Theorem 1 below provides a simple linear algebra approach for the computation of \mathbf{v} . First we need some auxiliary definitions.

Definition 4. Let $\{K_\ell : 1 \leq \ell \leq \#\mathcal{T}\}$ and $\{e_i : 1 \leq i \leq \#\mathcal{E}\}$ be two enumerations of the sets \mathcal{T} and \mathcal{E} respectively.

- (i) Given any element-wise constant vector field $\mathbf{w} = \sum_{\ell=1}^{\#\mathcal{T}} \mathbf{w}_{K_\ell} \mathbb{1}_{K_\ell}$, the following Index map gives the concatenation of its values as column vectors:

$$\text{Index} : \mathbf{H}(\Omega, \mathcal{T}) \rightarrow \mathbb{R}^{2\#\mathcal{T}}, \quad (\text{Index } \mathbf{w})(j) \stackrel{\text{def}}{=} \begin{cases} \mathbf{w}_{K_\ell} \cdot \hat{\mathbf{i}}, & j = 2\ell - 1, \\ \mathbf{w}_{K_\ell} \cdot \hat{\mathbf{j}}, & j = 2\ell. \end{cases} \quad (15)$$

- (ii) The **characterizing matrix** $A \in \mathbb{R}^{\#\mathcal{E} \times 2\#\mathcal{T}}$ of the triangulation \mathcal{T} has the entries of the normal outwards vectors $\hat{\mathbf{v}}_{K|L}$, organized as follows

$$A(i, j) \stackrel{\text{def}}{=} \begin{cases} \hat{\mathbf{v}}_{K_\ell|L_i} \cdot \hat{\mathbf{i}}, & j = 2\ell - 1, K_\ell \cap L_i \neq \emptyset, \\ \hat{\mathbf{v}}_{K_\ell|L_i} \cdot \hat{\mathbf{j}}, & j = 2\ell, K_\ell \cap L_i \neq \emptyset, \\ 0, & \text{otherwise.} \end{cases} \quad (16)$$

Theorem 1. Let \mathbf{v}_0, \mathbf{v} be the primary and master conservative velocity fields as defined in Equations (13), (14) respectively, then

$$\mathbf{v} = (\text{Index})^{-1} \left(I - A^T (AA^T)^{-1} A \right) \text{Index } \mathbf{v}_0. \quad (17)$$

PROOF. Note first that $\text{Index}[\mathbf{V}(\Omega, \mathcal{T})] = \ker(A)$, and therefore $\dim[\mathbf{V}(\Omega, \mathcal{T})] = \dim[\ker(A)] > 0$. Indeed, if $\mathbf{w} \in \mathbf{V}(\Omega, \mathcal{T})$, and $K, L_i \in \mathcal{T}$ are two triangles sharing the edge $e \in \mathcal{E}_{\text{itfc}}$, then the constraint in Definition (4) of $\mathbf{V}(\Omega, \mathcal{T})$ can be written as $\mathbf{a}_i \cdot \text{Index}(\mathbf{w}) = 0$ where \mathbf{a}_i is the i -th row vector of the matrix A . Since this holds for all $e \in \mathcal{E}_{\text{itfc}}$, this is equivalent to $A \text{Index}(\mathbf{w}) = \mathbf{0}$. The fact that $\ker(A)$ is not trivial, follows from the inequality $\#\mathcal{E}_{\text{itfc}} < \frac{3}{2} \#\mathcal{T} < 2\#\mathcal{T}$.

In order to obtain (17) from (14) it is enough to find a matrix representing the linear transformation $\text{Proj}_{\ker(A)}$. From standard linear algebra theory, the fundamental spaces of the matrix A satisfy

$$\ker(A) \perp \text{col}(A^T), \quad \ker(A) \oplus \text{col}(A^T) = \mathbb{R}^{2\#\mathcal{T}}, \quad (18)$$

where $\text{col}(A^T)$ is the column space of A^T and \oplus indicates the direct sum of vector spaces. Therefore, the projection is characterized by

$$\|\mathbf{x} - \text{Proj}_{\text{col}(A)}\mathbf{x}\| = \min \{ \|\mathbf{x} - A^T\mathbf{y}\| : \mathbf{y} \in \mathbb{R}^{\#\mathcal{E}} \}, \quad \text{for all } \mathbf{x} \in \mathbb{R}^{2\#\mathcal{T}},$$

with $\|\cdot\|$ the second order mean norm. From least squares standard theory we know that $\text{Proj}_{\text{col}(A)}\mathbf{x} = A^T(AA^T)^{-1}A\mathbf{x}$ for all $\mathbf{x} \in \mathbb{R}^{2\#\mathcal{T}}$. Finally, due to the orthogonality of the fundamental spaces in (18), we have that

$$\text{Proj}_{\ker(A)}\mathbf{x} = \left(I - A^T(AA^T)^{-1}A \right) \mathbf{x}, \quad \text{for all } \mathbf{x} \in \mathbb{R}^{2\#\mathcal{T}}.$$

From here the Identity (17) follows trivially.

Remark 1. A different approach would compute a numerical solution (\mathbf{v}_0, p_0) to Problem (8) using a dual mixed finite element method (see [9, 12]). In this case \mathbf{v}_0 already belongs to a Raviart-Thomas space $\mathbf{RT}_\ell(\Omega, \mathcal{T})$ of certain degree $\ell \geq 0$. In particular, the primary velocity field \mathbf{v}_0 is already numerically conservative; consequently, it is equal to the master conservative velocity field i.e., $\mathbf{v} = \mathbf{v}_0$ and, there is no need of the projection used in Theorem 1.

3.2. The lifting operator and the global velocity field \mathbf{u}

Our next step is to define, based on the master flow field \mathbf{v} , a new conservative three-dimensional flow field $\mathbf{u} \in \tilde{\mathbf{V}}(\Omega, \mathcal{T})$. The basic procedure consists in, for each element $K \in \mathcal{T}$, find an appropriate 3-D axis around which rigidly rotate horizontal vectors, so that \mathbf{v}_K ends up being parallel to the lifted triangular element K^ζ . In addition, the magnitude of the velocity vector, normal to the boundary of the element, is not altered and mass conservation is thus ensured.

Fix an element $K \in \mathcal{T}$ and let $\hat{\mathbf{n}}_K$ be the unit normal vector to the corresponding element $K^\zeta \in \tilde{\Gamma}_{\Omega, \mathcal{T}}$ as in Definition 3, see Figure 2. Let \mathbf{v}_K denote the value of the master flow field \mathbf{v} on K . If K^ζ is horizontal, we simply set $\mathbf{u}_K = \mathbf{v}_K$. Otherwise, we choose as a rotation axis the following vector

$$\hat{\mathbf{z}}_K \stackrel{\text{def}}{=} \frac{\hat{\mathbf{n}}_K \times \hat{\mathbf{k}}}{|\hat{\mathbf{n}}_K \times \hat{\mathbf{k}}|}. \quad (19)$$

The component of \mathbf{u}_K that is parallel to $\hat{\mathbf{z}}_K$ is set equal to that of \mathbf{v}_K , namely $\text{Proj}_{\hat{\mathbf{z}}_K}(\mathbf{u}_K) = \text{Proj}_{\hat{\mathbf{z}}_K}(\mathbf{v}_K)$. Now, let Λ_K be the plane normal to $\hat{\mathbf{z}}_K$, and let θ_K be the angle formed from $\hat{\mathbf{k}}$ to $\hat{\mathbf{n}}_K$ on the plane Λ_K . The component of \mathbf{u}_K perpendicular to $\hat{\mathbf{z}}_K$ is then taken equal to the vector obtained from rotating $\text{Proj}_{\Lambda_K}(\mathbf{v}_K)$ by the angle θ_K .

The **lifting operator map**, $F_K : \mathbb{R}^2 \rightarrow \mathbb{R}^3$, $\mathbf{v}_K \mapsto \mathbf{u}_K$ is linear and it is explicitly written as:

$$\mathbf{u}_K \stackrel{\text{def}}{=} \begin{bmatrix} 1 - \frac{n_1^2}{1+n_3} & -\frac{n_1 n_2}{1+n_3} \\ -\frac{n_1 n_2}{1+n_3} & 1 - \frac{n_2^2}{1+n_3} \\ -n_1 & -n_2 \end{bmatrix} \mathbf{v}_K \stackrel{\text{def}}{=} F_K \mathbf{v}_K, \quad \hat{\mathbf{n}}_K = \begin{bmatrix} n_1 \\ n_2 \\ n_3 \end{bmatrix}. \quad (20)$$

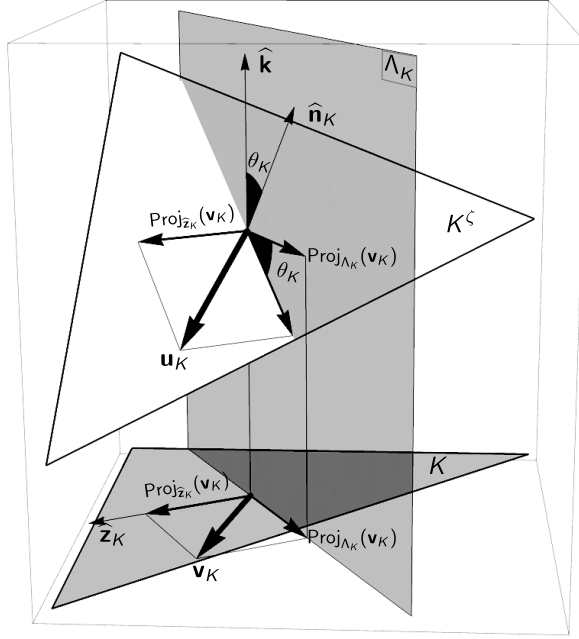


Figure 2: Schematics of the lifting of the conservative field \mathbf{v}_K to the global velocity field \mathbf{u}_K for a fixed element K .

The **global velocity field** \mathbf{u} is then defined by

$$\mathbf{u}(\mathbf{x}) \stackrel{\text{def}}{=} \sum_{K \in \mathcal{T}} \mathbf{u}_K \mathbb{1}_K(\mathbf{x}), \quad \mathbf{x} \in \Omega, \quad (21)$$

Remark 2. (i) The construction of the lifting operator $F \stackrel{\text{def}}{=} \sum_{K \in \mathcal{T}} F_K \mathbb{1}_K(\mathbf{x})$, $\mathbf{x} \in \Omega$ (20) is based on preserving the magnitudes of the vectors on every direction normal to the boundary of K^ζ . Consequently, since the master conservative field \mathbf{v} belongs to $\mathbf{V}(\Omega, \mathcal{T})$ then, its lifting \mathbf{u} belongs to $\tilde{\mathbf{V}}(\Omega, \mathcal{T})$, i.e. \mathbf{u} is conservative.

(ii) Given two master conservative fields $\mathbf{v}_1, \mathbf{v}_2 \in \mathbf{V}(\Omega, \mathcal{T})$, a direct calculation shows that

$$\mathbf{v}_1(\mathbf{x}) \cdot \mathbf{v}_2(\mathbf{x}) = \mathbf{u}(\mathbf{v}_1, \mathbf{x}) \cdot \mathbf{u}(\mathbf{v}_2, \mathbf{x}) \quad \text{for all } \mathbf{x} \in \Omega. \quad (22)$$

3.3. Mean streamline length

Within each lifted element K^ζ , the streamlines of the field \mathbf{u} are parallel. In the context of energy dissipation discussed in Section 5, we will need the average length $\mathbf{d}_K(\mathbf{u})$, of such streamlines.

Consider first the triangle $K \in \mathcal{T}$ shown in Figure 3. It is an elementary fact that the average streamline length within K of the field \mathbf{v}_K is equal to $d_K(\mathbf{v}) = \frac{1}{2} \|\mathbf{y}_K(\mathbf{v})\|$ where $\|\mathbf{y}_K(\mathbf{v})\|$ is the maximum length of segments parallel to \mathbf{v}_K contained in K . Clearly $\mathbf{y}_K(\mathbf{v}) = \alpha_K \mathbf{v}_K$ for some $\alpha_K > 0$. The desired distance is then obtained by applying the operator F_K of (20) to \mathbf{y}_K ,

$$\mathbf{d}_K(\mathbf{u}) = \frac{1}{2} \|F_K \mathbf{y}_K(\mathbf{v})\| = \frac{1}{2} \alpha_K \|\mathbf{u}_K\|. \quad (23)$$

We now provide an algorithm to compute α_K . Let $\mathbf{e}_1, \mathbf{e}_2, \mathbf{e}_3$ denote the edges of element K , and consider the products $f_i = (\hat{\mathbf{v}}_{\mathbf{e}_i} \cdot \mathbf{v}_K)$. If any of the f_i equals zero, then there is an edge vector \mathbf{e}_i parallel to \mathbf{v}_K and we make $\mathbf{y}_K(\mathbf{v}) = \mathbf{e}_i$, $\alpha_K = \|\mathbf{e}_i\|/\|\mathbf{v}_K\|$. Otherwise the f_i satisfy the following property: there is a unique edge $\mathbf{e}_{v,1}$ for which its corresponding $f_{v,1} = (\hat{\mathbf{v}}_{\mathbf{e}_{v,1}} \cdot \mathbf{v}_K)$ has sign different from the other two, namely $f_{v,1}$ is the unique strictly negative or strictly positive number among f_1, f_2, f_3 . The vector \mathbf{v}_K enters or exits K through the edge $\mathbf{e}_{v,1}$

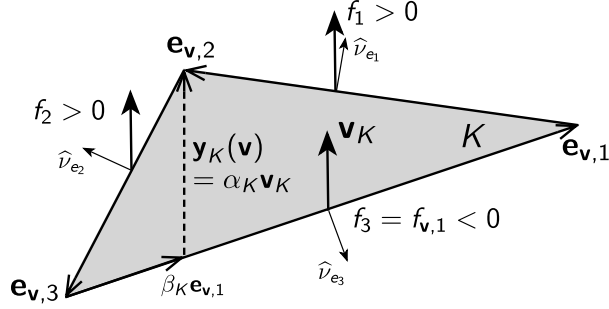


Figure 3: Calculation of the mean streamline length of the field \mathbf{v}_K . The vector $\mathbf{y}_K(\mathbf{v}) = \alpha_K \mathbf{v}_K$ is shown as dashed. In this case the \mathbf{y}_K enters K through $e_{v,1}$ because $f_3 = f_{v,1} < 0$.

according to $\text{sign}(f_{v,1})$. Let $\mathbf{e}_{v,1}, \mathbf{e}_{v,2}, \mathbf{e}_{v,3}$ denote the edge vectors of K transversing ∂K in the counter-clockwise direction and starting with the selected edge $e_{v,1}$. There exist unique positive constants α_K, β_K such that

$$\mathbf{e}_{v,3} + \beta_K \mathbf{e}_{v,1} - \text{sign}(f_{v,1}) \alpha_K \mathbf{v}_K = \mathbf{0}. \quad (24)$$

4. Transport along the surface

In this section we derive a stochastic model for the linearized transport of a solute which is being advected along the surface by the global velocity field \mathbf{u} . The starting point is the linear transport equation for a solute of concentration per unit volume $c(\mathbf{x}, t)$ which is being advected by the velocity field \mathbf{u} and initially distributed according to an initial concentration c_0 :

$$\partial_t c(\mathbf{x}, t) + \text{div}(\mathbf{u}c)(\mathbf{x}, t) = 0 \quad c(\mathbf{x}, 0) = c_0(\mathbf{x}), \quad \mathbf{x} \in \tilde{\Gamma}_{\Omega, \mathcal{T}}. \quad (25)$$

Upon discretization of the surface by the triangulation \mathcal{T} and integration over each element, the following approximation to (25) is obtained

$$\frac{dc}{dt} = Qc(t), \quad c(0) = c^{(0)}, \quad (26)$$

where now \mathbf{c} and $\mathbf{c}^{(0)}$ denote vectors in $\mathbb{R}^{\#\mathcal{T}_{\text{ext}}}$ with entries given by the total mass of solute over each element,

$$c_K(t) = \int_{K^\zeta \times D} c(\mathbf{x}, t) d\mathbf{x}, \quad c_K^{(0)} = c_K(0). \quad (27)$$

The integration is carried over the volume $K^\zeta \times D$ where $0 < D \ll 1$ is the depth of flow (i.e. the thickness of the fissure) and is assumed to be constant throughout. The matrix $Q \in \mathbb{R}^{\#\mathcal{T}_{\text{ext}} \times \#\mathcal{T}_{\text{ext}}}$ in (26) corresponds to the discretized version of the divergence operator, and is given by

$$Q_{K,K} \stackrel{\text{def}}{=} - \sum_{\substack{L \in \mathcal{T}_{\text{ext}} \\ |\partial L \cap \partial K| > 0}} \frac{\sigma_{K|L}^\zeta}{|K^\zeta|} (\mathbf{u}_K \cdot \hat{\nu}_{K|L})^+, \quad K \in \mathcal{T}_{\text{ext}}; \quad (28)$$

$$Q_{K,L} \stackrel{\text{def}}{=} \frac{\sigma_{K|L}^\zeta}{|K^\zeta|} (\mathbf{u}_K \cdot \hat{\nu}_{K|L})^+, \quad \text{if } K, L \in \mathcal{T}_{\text{ext}}, K \neq L, |\partial K \cap \partial L| > 0, \quad (29)$$

where $z^+ = \max\{z, 0\}$ for $z \in \mathbb{R}$.

The solution to (26) is

$$\mathbf{c}(t) = \exp(Qt) \mathbf{c}^{(0)} \stackrel{\text{def}}{=} T(t) \mathbf{c}^{(0)}, \quad t \geq 0. \quad (30)$$

Remark 3. (i) Each entry of the matrix Q has units of fraction of solute mass per unit time. The rows corresponding to elements in $\mathcal{T}_{\text{ext}} - \mathcal{T}$ contain zero in all its entries.

(ii) Note that because of the construction of the global velocity field, the terms $(\mathbf{u}_K \cdot \widehat{\nu}_{K|L})$ can be replaced throughout (28) by the dot product $(\mathbf{v}_K \cdot \widehat{\nu}_{K|L})$ of vectors in \mathbb{R}^2 .

(iii) In contrast, the cross sectional area used in the computation of Q must be computed with the distance σ_e^ζ .

It is important to point out that, in the case where $\sum_{K \in \mathcal{T}} c_K^{(0)} = 1$, the concentration $\mathbf{c}(t)$ in (30) can be understood as the distribution of a stochastic process $X = \{X(t) : t \geq 0\}$ initially distributed according to $\mathbf{c}^{(0)}$ and with phase space given by the elements of \mathcal{T}_{ext} . Namely,

$$c_K(t) = \mathbb{P}(X(t) = K | X(0) \sim \mathbf{c}^{(0)}) \quad (31)$$

and $X(t)$ thus represents a random model for the position of an individual molecule of the solute being advected. The elements in $\mathcal{T}_{\text{ext}} - \mathcal{T}$ are absorbing states. The randomness in this stochastic process comes from the uncertainty in the geometry of the fissure which is reflected in the approximation of \mathbf{u}_K to the real velocity field on the points of the surface. In this context, the matrix Q is the “infinitesimal generator” of X while the family of “transition probability matrices” of the process $\{T(t) : t \geq 0\}$, defined in Identity 30, is given by

$$T_{K,L}(t) \stackrel{\text{def}}{=} \mathbb{P}(X(t) = L | X(0) = K), \quad K, L \in \mathcal{T}_{\text{ext}}. \quad (32)$$

See Chapter IV in [5].

4.1. The geometry of transport

The matrix Q provides a description of the rates of transport forced by the velocity field \mathbf{u} along the surface. It therefore gives detailed information about which parts of the surface are accessible to the flow from any initial position. To be precise, let \widetilde{Q} be the transition probability matrix of the Markov chain associated to X (see [5], V.5)

$$\widetilde{Q}_{K,L} = \frac{Q_{K,L}}{-Q_{K,K}} \text{ if } Q_{K,K} \neq 0, \quad \widetilde{Q}_{K,L} = 0 \text{ if } Q_{K,K} = 0, \quad K \neq L; \quad (33)$$

$$\widetilde{Q}_{K,K} = 0 \text{ if } Q_{K,K} \neq 0, \quad \widetilde{Q}_{K,K} = 1 \text{ if } Q_{K,K} = 0 \quad (34)$$

and let \mathcal{G} be the directed weighted graph whose adjacency matrix is \widetilde{Q} . We will refer to \mathcal{G} as the “flow graph” associated with the velocity field \mathbf{u} .

We say that the element K is upstream from the element L and denote it by $K \rightarrow L$, if $(\widetilde{Q}^n)_{K,L} > 0$ for some $n \geq 1$, or equivalently, there exists a path in \mathcal{G} connecting K with L . It follows from the standard theory of Markov processes that $K \rightarrow L$ implies $T_{K,L}(t) > 0$ for all $t > 0$. In other words, it is likely for a particle originally within triangle K to be transported to the element L .

A particular feature of the flow graph \mathcal{G} generated by \mathbf{u} is that it is a forest, a collection of trees similar to a river network driven by the gravitational potential over the landscape.

Theorem 2. *The unique cycles in \mathcal{G} have length one. In particular, no element $K \in \mathcal{T}$ is downstream of itself.*

PROOF. *First we observe that for any $\mathbf{v} \in \mathbf{V}(\Omega, \mathcal{T})$ there exists $q \in E(\Omega, \mathcal{T})$ such that $\mathbf{v} = -\mathbf{grad} \, q$ (see Identity (5)). Now we proceed to prove the result by way of contradiction, let $\{L_i : 0 \leq i \leq j\}$ be a cycle in \mathcal{G} . Define $K \stackrel{\text{def}}{=} L_0 = L_j$ and denote by $e_i = L_{i-1}|L_i$, $1 \leq i \leq j$ the sequence of edges joining subsequent elements of the cycle. Also define the midpoints \mathbf{x}_i of e_i and the unitary vectors $\widehat{\nu}_{e_i}$ outwards L_{i-1} and orthogonal to e_i . Notice that since L_0, L_1, \dots, L_j are successors then $Q_{L_{i-1}, L_i} > 0$ for $i = 1, 2, \dots, j$. In particular, since $\mathbf{v}_{L_i} = -\mathbf{grad} \, q|_{M_i}$, due to the definition of Q_{M_{i-1}, M_i} this implies that $q(\mathbf{x}_{i-1}) \not\leq q(\mathbf{x}_i)$ for all $i = 1, 2, \dots, j$. Therefore, because of the continuity of q it follows that*

$$q(\mathbf{x}_0) \not\leq q(\mathbf{x}_1) \not\leq \dots \not\leq q(\mathbf{x}_j) \not\leq q(\mathbf{x}_0).$$

Since this is a contradiction, the proof is complete.

4.2. The time to reach the boundary

One advantage of the stochastic formulation is that we can explicitly consider dynamic quantities regarding the motion of individual solute particles, and their aggregated properties. Most significantly, consider the random time it takes a particle to reach $\partial\mathcal{T}$,

$$\tau = \inf\{t \geq 0 : X(t) \in \partial\mathcal{T}\} \quad (35)$$

and its distribution conditioned to having started within element $K \in \mathcal{T}$, which can be characterized via

$$\Phi_K(t) \stackrel{\text{def}}{=} \mathbb{P}(\tau > t | X(0) = K), \quad K \in \mathcal{T}. \quad (36)$$

The states in $\mathcal{T}_{\text{ext}} - \mathcal{T}$ are absorbing, then it follows that

$$\Phi_K(t) = \sum_{L \in \mathcal{T}} T_{K,L}(t), \quad \Phi(t) = T(t)\mathbf{1}_{\mathcal{T}} \quad (37)$$

where, in the second equation, $\Phi(t)$ denotes the vector with entries $\{\Phi_K(t) : K \in \mathcal{T}\}$ and $\mathbf{1}_{\mathcal{T}}$ is the vector with ones on the entries corresponding to the triangles in \mathcal{T} and zeros everywhere else, see [5] IV.10.

Since τ is a positive random variable, its expectation can be computed directly from Φ . Define

$$\Psi_K \stackrel{\text{def}}{=} \mathbb{E}(\tau | X(0) = K), \quad (38)$$

and let Ψ be the vector with entries $\{\Psi_K(t) : K \in \mathcal{T}\}$. One thus arrives to the following useful formula:

$$\Psi = \int_0^\infty \exp(Qt) \mathbf{1}_{\mathcal{T}} dt. \quad (39)$$

Even though it can be shown that $\Psi < \infty$, no closed formula is possible for the integral in (39) because Q is by construction, a singular matrix.

5. Applications and Numerical Examples

In this section we present three important applications of constructed the flow field. The first one is the computation of the preferential flow direction for a layered medium. The second one is a computation of energy dissipation hosted on the surface. The third one is a computation of probable stream lines through the surface.

5.1. Preferential Flow Direction

Let \mathbf{u} be the global velocity field defined in (21). The **preferential flow direction** of the medium is given by

$$\mathbf{m}[\mathbf{u}] \stackrel{\text{def}}{=} \frac{1}{|\Gamma|} \sum_{K \in \mathcal{T}} |K^\zeta| \mathbf{u}_K. \quad (40)$$

The vector $\mathbf{m}[\mathbf{u}] \in \mathbb{R}^3$ is an estimate of the mean velocity of whole fissure.

5.2. Energy Dissipation

Three separate physical mechanisms of energy dissipation are considered: Curvature, Friction and Gravity. For each mechanism, a functional of energy dissipation is constructed for computational purposes.

Definition 5. The **energy dissipation rate due to curvature** is given by the total kinetic energy of such deviation, weighted according the flow rate (see [6, 7]), i.e.

$$U_{\text{curv}}(\mathbf{u}) \stackrel{\text{def}}{=} \frac{1}{2} \rho D \sum_{K \in \mathcal{T}} \sum_{\substack{L \in \mathcal{T} \\ |\partial L \cap \partial K| > 0}} (|K^\zeta| \tilde{Q}_{K,L} + |L^\zeta| \tilde{Q}_{L,K}) \|(\mathbf{u}_K \cdot \hat{\nu}_{K|L}) \hat{\nu}_{K|L} - (\mathbf{u}_L \cdot \hat{\nu}_{L|K}) \hat{\nu}_{L|K}\|^2. \quad (41)$$

Here, ρ is the density of the fluid, g is the gravity.

Remark 4. (i) Notice that although the conservative flow field \mathbf{v} is continuous in the normal direction across the interfaces $e \in \mathcal{E}_{\text{itfc}}$. Due to the lifting, the vertical component of the global flow field \mathbf{u} deviates from one element to its neighbor, because of the curvature of the surface Γ . Therefore, certain amount of energy has to be invested for the fluid to reach the configuration of its neighbor, the Identity (41) quantifies the total of this needed energy per unit time.

(ii) Observe that the factor $D(|K^\zeta| \tilde{Q}_{K,L} + |L^\zeta| \tilde{Q}_{L,K})$ in the Identity (41) quantifies the fraction of volume per unit time that crosses the edge $K|L$ because one of the summands is necessarily null, i.e. $\tilde{Q}_{K,L} \tilde{Q}_{L,K} = 0$.

Next we define the friction and gravity dissipation energy functionals. Recall that the dissipation head of mechanical energy due to friction (see [25]) is given by the Darcy-Weisbach type equation

$$\gamma \frac{l}{D} \frac{1}{2g} \|\mathbf{u}\|^2. \quad (42)$$

Here γ is a dimensionless friction coefficient depending on the material of the walls of the fissure and the viscosity of the fluid, l is the average length of the fluid path, and D is the layer height and $\|\mathbf{u}\|$ is the average magnitude of the velocity. In order to convert the head (42) into a dissipation rate we will need the total discharge flowing out of element K^ζ defined as:

$$\mathbf{q}_K \stackrel{\text{def}}{=} -D|K^\zeta| Q_{K,K} \quad (43)$$

where $Q_{K,K}$ is defined in (28).

Definition 6. The total **energy dissipation rate due to friction** is given by

$$U_{\text{fric}}(\mathbf{u}) \stackrel{\text{def}}{=} \frac{1}{2} \rho \gamma \sum_{K \in \mathcal{T}} \mathbf{q}_K \frac{\mathbf{d}_K(\mathbf{u})}{D} \|\mathbf{u}_K\|^2. \quad (44)$$

Here \mathbf{q}_K is the discharge rate outwards the element K^ζ defined in the Identity 28 and $\mathbf{d}_K(\mathbf{u})$ is the mean streamline length constructed in section 3.3.

For the quantification of the energy dissipation due to gravity, we fix $K \in \mathcal{T}$ and compute the increase or decrease of potential energy experienced by the flow field inside K . The mean change in potential energy due to a layer of flow moving in the direction \mathbf{u}_K can be computed as $\frac{1}{2}(\mathbf{F}\mathbf{y}_K) \cdot \hat{\mathbf{k}} = \frac{1}{2}\alpha_K(\mathbf{u}_K \cdot \hat{\mathbf{k}})$ where $\frac{1}{2}\tilde{y}_K(\mathbf{v}) = \frac{1}{2}\alpha_K\mathbf{v}_K$ is the mean streamline length found in section 3.3. We thus define:

Definition 7. The total **variation of potential energy rate** is given by

$$U_{\text{grav}}(\mathbf{u}) \stackrel{\text{def}}{=} \frac{1}{2} \rho g \sum_{K \in \mathcal{T}} \mathbf{q}_K \alpha_K (\mathbf{u}_K \cdot \hat{\mathbf{k}}) \quad (45)$$

Remark 5. Notice that unlike the physical mechanisms of curvature and friction where U_{curv} , U_{fric} are quantities of energy dissipation, the functional U_{grav} may report an increment of potential energy depending on \mathbf{v} .

5.3. Numerical Experiments

Here we present two numerical examples to illustrate the measurement of the physical quantities proposed throughout this section as well as the boundary reaching times. The two examples below correspond to different surfaces, in each case we perform two experiments, one with a null pressure potential, i.e., $P = 0$ and the other with a logarithmic pressure potential $P = 4000 \log((x - h)^2 + (y - k)^2)$, corresponding to a well centered at the point $C = \begin{pmatrix} h \\ k \end{pmatrix}$; notice that the pressure potential is the fundamental solution of the 2-D Laplace equation at the point C . For the graphics, we display side by side the potentials $\rho g \zeta$, $\rho g \zeta + P$, below each other the associated conservative flow fields are depicted and finally, the corresponding expected boundary reaching times

per element are shown. The experiments are executed in a MATLAB script and use a Delaunay triangulation, composed of 322 elements for the first example and 1046 elements for the second example, where the vertices were generated randomly.

Due to the scales of the phenomenon we choose the CGS system of units, for both examples we choose the values: water density $\rho = 100 \text{ kg/m}^3$, gravity $g = 9.81 \text{ m/s}^2$, water layer thickness $D = 0.01 \text{ m}$, Darcy-Weishbach coefficient $\gamma = 0.03$ and flow resistance $a = 1.3071 * 10^3 \text{ m}^3 \text{ s/g}$, the geometric domain is the unit square i.e., $G = [0, 1]^2$. In contrast, the numerical values describing the overall behavior of the surface, displayed in Tables 1, 2 of Examples 1 and 2 respectively, are presented in the CGS system, due to its scale. These values are the average velocity $\mathbf{m}[\mathbf{u}(\mathbf{v})]$, the energy losses U_{curv} , U_{fric} , U_{grav} and the average expected time (average of the elements' expected time), denoted by $\mathbf{m}[\mathbb{E}(\tau|X(0) = K)]$. We also stress that in this context, positive amounts of energy indicate dissipation, while a negative sign means that such quantity is still available in the form of kinetic energy.

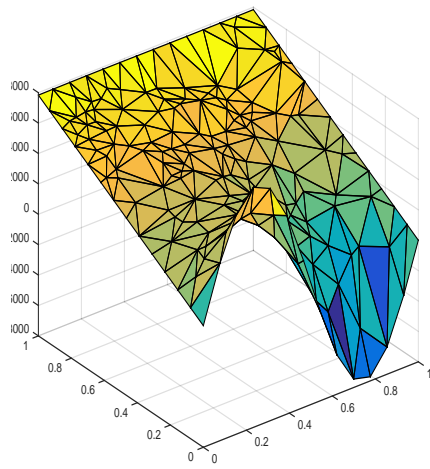
Example 1. The first example is for verification purposes. The surface is given by the plane $\zeta : G \rightarrow \mathbb{R}$, $\zeta(x, y) = 0.8(\sin(2\pi x) \exp(-2\pi y) + y)$. For the first experiment we set $P \equiv 0$ and for the second, a pressure potential $P = 4000 \log((x - 110)^2 + (y + 10)^2)$ i.e., an extraction well beyond the upper left corner of the graphic. Notice that both potentials are harmonic functions (see Figures 4 (a) and (b) respectively), therefore the master velocity fields are a multiple the corresponding gradients and the global conservative fields are the lifting of such gradients multiplied by $\frac{1}{a}$. These facts can be observed on Figures 4 (c) and (d). Also notice that the expected boundary reaching times are consistent with the a-priori intuitive notion as Figures 4 (e) and (f) show. The next table summarizes the overall behavior of the surface for both potentials.

Experiment	$\mathbf{m}[\mathbf{u}(\mathbf{v})]$ [cm/s]	U_{curv} [erg/s]	U_{fric} [erg/s]	U_{grav} [erg/s]	Energy Balance [erg/s]	$\mathbf{m}[\mathbb{E}(\tau X(0) = K)]$ [s]
Gravity driven only	$\begin{pmatrix} 0.0028 \\ -0.3548 \\ -1.0626 \end{pmatrix}$	231.7744	2123.0304	-103578.4	-101223.7	134
Gravity and pressure driven	$\begin{pmatrix} -0.4228 \\ 0.0236 \\ -0.83512 \end{pmatrix}$	262.4044	2142.613	-70541.36	-68136.34	105

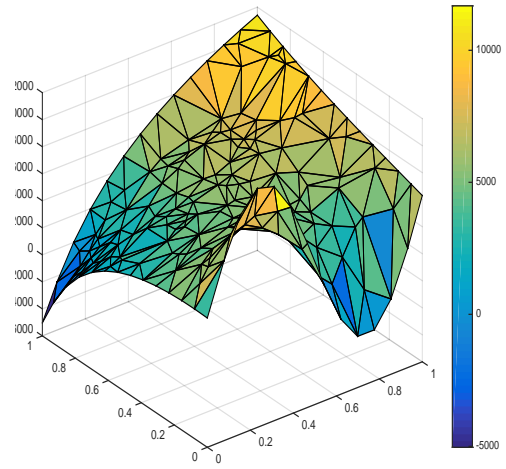
Table 1: Example 1: Energy Dissipation Table, 322 Elements.

From the table above it follows that for both potentials, the main driving force is the gravity. For the first case, the order of scales states that $U_{\text{curv}} \ll U_{\text{fric}} \ll U_{\text{grav}}$. In the second case the well is meant to force the flow uphill, which is done up to an extent, this is reflected as the value of U_{grav} contracts in 32 percent approximately, while U_{curv} and U_{fric} do not change significantly with respect to itself hence, the order of scales is changed to $U_{\text{curv}} \ll U_{\text{fric}} \sim U_{\text{grav}}$. Finally, it is observed that the average expected reaching time decreases in 20 percent from the first to the second case as now there are two main evacuation points.

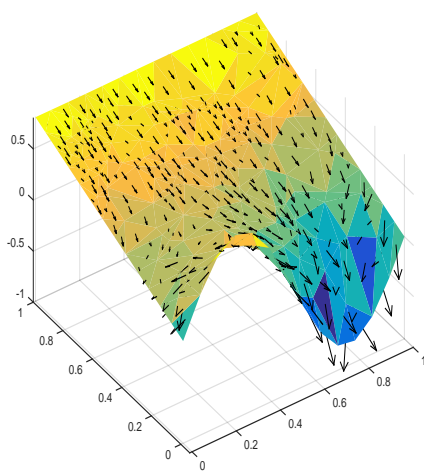
Example 2. The second example explores a more complex scenario. The surface is given by the function $\zeta : G \rightarrow \mathbb{R}$, $\zeta(x, y) = 0.5x \sin(2\pi x) + 0.5x + 0.075 \sin(6\pi y)$. Clearly, this function has significant more curvature and surface than the previous one, aside from not been harmonic. Again, for the first experiment we set $P \equiv 0$ and for the second, a pressure potential $P = 4000 \log((x - 110)^2 + (y - 110)^2)$ i.e., an extraction well beyond the upper right corner of the graphic. The well is placed near the highest point of the surface to counteract the dominant effect of the gravity as it sees in Figures 5 (a) and (b). For the gravity driven flow the velocity field (see Figure 5 (c)) attains the highest velocities and consequently the highest discharge rates in the valleys of the surface as expected. In the second case, due to the presence of the well the flow preference is split in two



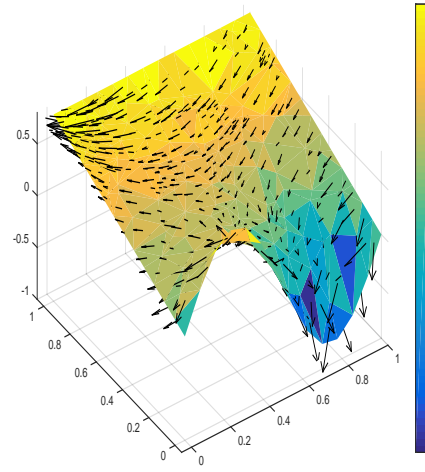
(a) Forcing Potential Surface $\rho g \zeta$.



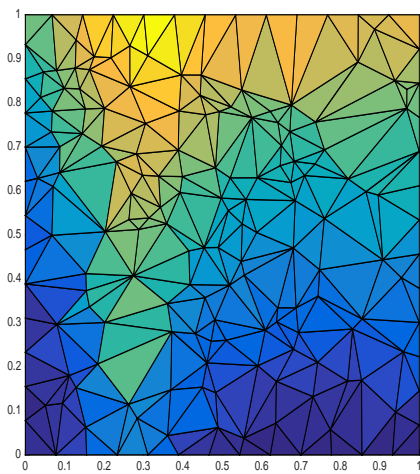
(b) Forcing Potential Surface $\rho g \zeta + P$.



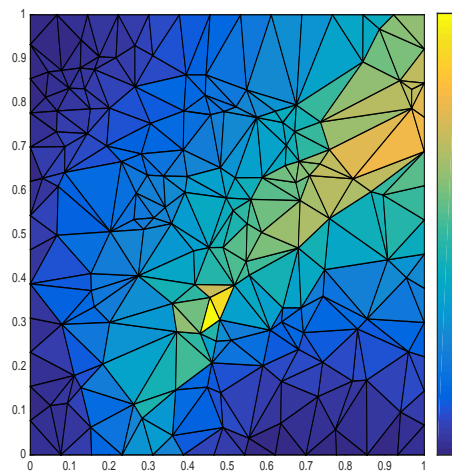
(c) Flow Field gravity driven flow.



(d) Flow Field gravity and pressure driven flow.



(e) Expected boundary reaching times gravity driven flow.



(f) Expected boundary reaching times gravity and pressure driven flow.

Figure 4: First example for verification purposes

portions, one fraction moves towards the well, the other through the lower valleys and, the highest velocities are attained near the main evacuation points, see Figure 5 (d). Finally, the expected reaching times agree with the intuitive notion, in the first case the highest values are in the top peaks and the lowest values near the boundary and the lower valleys, see Figure 5 (e). In the second case, the lowest expected reaching times occur near the major evacuation points the lowest take place on the peaks away from both evacuation points, see Figure 5 (f).

Experiment	$\mathbf{m}[\mathbf{u}(\mathbf{v})]$ [cm/s]	U_{curv} [erg/s]	U_{fric} [erg/s]	U_{grav} [erg/s]	Energy Balance [erg/s]	$\mathbf{m}[\mathbb{E}(\tau X(0) = K)]$ [s]
Gravity driven only	$\begin{pmatrix} 0.0086 \\ -0.2650 \\ -0.3012 \end{pmatrix}$	94.70545	214.7014	-30869.39	-30559.98	198
Gravity and pressure driven	$\begin{pmatrix} 0.3868 \\ 0.2218 \\ -0.1802 \end{pmatrix}$	273.5967	531.7068	-16713.18	-15907.87	177

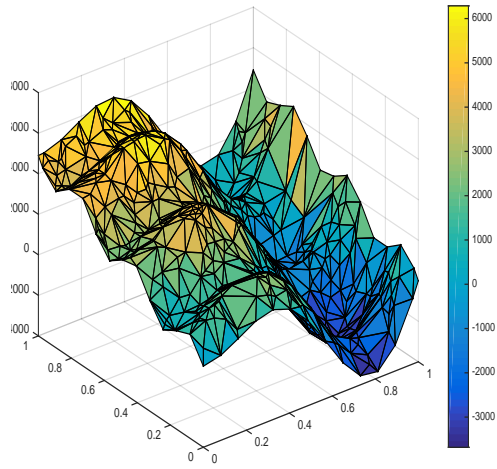
Table 2: Example 2: Energy Dissipation Table, 1046 Elements.

We summarize in the Table 2 below the overall behavior of the surface for both potentials. Again it follows that for both potentials, dominant effect is the gravity. In the first case the order of scales states that $U_{\text{curv}} \sim U_{\text{fric}} \ll U_{\text{grav}}$. In the second case the well pulls the flow uphill towards the highest point consequently, the value of U_{grav} contracts around 45 percent, while U_{curv} and U_{grav} increase drastically around 300 and 100 percent respectively but preserving the same order of scales $U_{\text{curv}} \sim U_{\text{fric}} \ll U_{\text{grav}}$. It also follows that the increase of these two effects come from the fact that the new stream lines travel along more curved and therefore longer paths. Finally, it is observed that the average expected reaching time decreases in only 10 percent from the first to the second case; although there are now two main evacuation points, the top point demands more travel time due to the increase in the length of the stream lines and the magnitudes of the flow field.

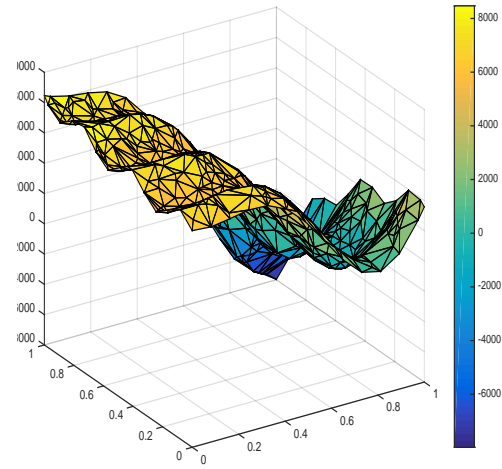
6. Conclusions

The present work yields several conclusions listed below

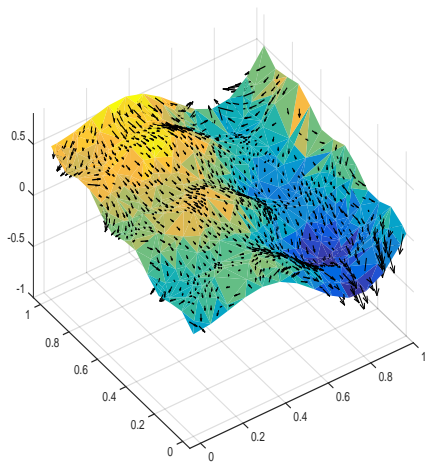
- (i) We proposed a method aimed to describe the flow on the fissures embedded in a porous medium and also to measure its impact in terms of energy dissipation and transport phenomena.
- (ii) Unlike previous achievements, the present work is capable of describing explicitly the flow field on the fissure under mild hypotheses. Moreover, here the geometry of the manifold plays a central role for the quantifications we seek.
- (iii) Our approach is consistent and applicable to real case scenarios as pointed out in the introduction, because the available data for geological structures are discrete, therefore an interpolation process has to be done and the uncertainty coming from the knowledge of the geometry needs to be accounted for.
- (iv) The proposed method is remarkably simple as it is in essence a composition of linear operators and yet it computes accurately the analyzed phenomena and can be extended to other physical aspects. This simplicity is precisely its main fortitude because it makes it computationally efficient and thus fit for large scale computations, when it comes to simulate highly fractured media.
- (v) The values of energy dissipation may not seem important in the presented experiments and they are of lower order scale with respect to the gravity however, at the field scale these effects become important as they



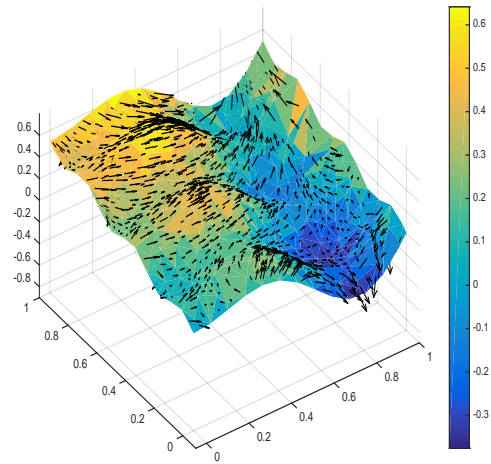
(a) Forcing Potential Surface $\rho g \zeta$.



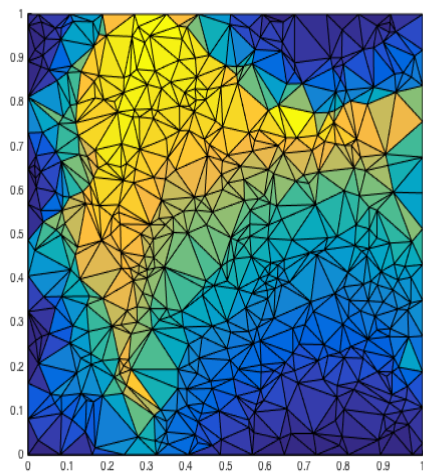
(b) Forcing Potential Surface $\rho g \zeta + P$.



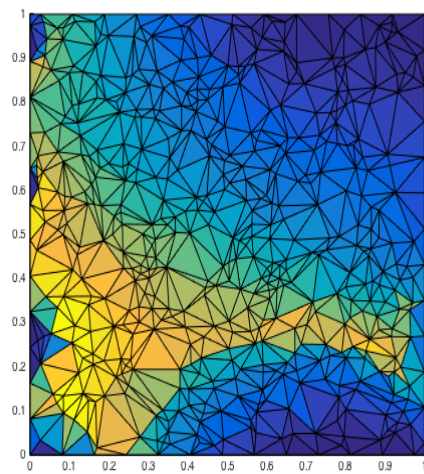
(c) Flow Field gravity driven flow.



(d) Flow Field gravity and pressure driven flow.



(e) Expected boundary reaching times gravity driven flow.



(f) Expected boundary reaching times gravity and pressure driven flow.

Figure 5: Second example for experimental purposes

add up the losses from a large number of extended fissures. In addition the average velocity for a given surface $\mathbf{m}[\mathbf{u}(\mathbf{v})]$ defines what would the preferential flow direction of the medium would be, should there be only one embedded fissure. It follows that for a highly fractured medium the preferential flow direction (see [11] for a different approach) is determined by the mean flow directions of each surface weighted vs. the corresponding discharge rate they host, relative to the total discharge rate along the cracks network.

- (vi) A natural question would be the extension of the method to a different interpolation method for the geometry, e.g. using splines rather than linear affine functions. However, this approach introduces a lot of computational complexity both on the geometric interpolation itself and in the construction of a conservative tangential flow analogous to the one furnished by the operator F defined in Identity (21). Hence, despite its mathematical interest, such approach is not viable for large scale simulations as the built-in complexity introduces issues such as ill-conditioned matrices, problems of numerical stability, poor quality of the numerical solutions and high computational costs.

Acknowledgments

This work was supported by the project HERMES 27798 from Universidad Nacional de Colombia, Sede Medellín.

References

- [1] ARBOGAST, T. & BRUNSON, D. (2007) A computational method for approximating a Darcy-Stokes system governing a vuggy porous medium. *Computational Geosciences*, **11**, No 3, 207–218.
- [2] ARBOGAST, T., DOUGLAS, JR, J. & HORNUNG, U. (1990) Derivation of the double porosity model of single-phase flow via homogenization theory. *SIAM Journal of Mathematical Analysis*, **21**, 823–836.
- [3] ARBOGAST, T. & LEHR, H. (2006) Homogenization of a Darcy-Stokes System Modeling Vuggy Porous Media. *Computational Geosciences*, **10**, No 3, 291–302.
- [4] BARENBLATT, G., ZHELTOV, I. & KOCHINA, I. (1960) Basic concepts in the theory of seepage and homogeneous liquids in fissured rocks. *Journal of Applied Mechanics*, **24**, 1286–1303.
- [5] RABI N. BHATTACHARYA & EDWARD C. WAYMIRE (2009) *Stochastic Processes With Applications*, Classics in Applied Mathematics, Vol. 61, Society for Industrial & Applied Mathematics, PA.
- [6] BATCHELOR, G. (2002) *An Introduction to Fluid Dynamics*, Cambridge Mathematical Library. Cambridge University Press, New York.
- [7] BEAR, J. (1988) *Dynamics of Fluids in Porous Media*. Dover Publications Inc., New York.
- [8] BRADJI, A. & HERBIN, R. (2006) On the discretization of the coupled heat and electrical diffusion problems. *Numerical Methods and Applications: 6th International Conference, NMA 2006, Borovets, Bulgaria, Revised Papers*. Springer, pp. 1–15.
- [9] D. BRAESS *Finite Elements. Theory fast solvers and applications in solid mechanics*, 3rd Ed, Cambridge University Press, Cambridge 2007.
- [10] COFFIELD, JR, D. J. & SPAGNUOLO, A. M. (2003) Analysis of a multiple-porosity model for a single-phase flow through naturally fractured porous media. *Journal of Applied Mathematics*, **2003**:7, 327–364. [dx.doi.org/10.1155/S1110757X03205143](https://doi.org/10.1155/S1110757X03205143).
- [11] FIORI, A. & JANKOVIC, I. (2012) On preferential flow, channeling and connectivity in heterogeneous porous formations. *Mathematical Geosciences*, **44**, No 2, 133–145. [dx.doi.org/10.1007/s11004-011-9365-2](https://doi.org/10.1007/s11004-011-9365-2).
- [12] GATICA G. (2014) *A Simple Introduction to the Mixed Finite Element Method*. SpringerBriefs in Mathematics. Springer International Publisher; 1 edition, New York.
- [13] LESINIGO, M., D'ANGELO, C. & QUARTERONI, A. (2011) A multiscale Darcy-Brinkman model for fluid flow in fractured media. *Numerische Mathematik*, **117**, 717–752. [dx.doi.org/10.1007/s00211-010-0343-2](https://doi.org/10.1007/s00211-010-0343-2).
- [14] LEVEQUE RANDALL. (2002) *Finite Volume Methods for Hyperbolic Problems*. Cambridge texts in Applied Mathematics. Cambridge University Press, New York.
- [15] McLAREN, R., FORSYTH, P., SUDICKY, E., VANDERKWAAK, J., SCHWARTS, F. & KESSLER, J. (2000) Flow and transport in fractured tuff at Yucca Mountain: numerical experiments on fast preferential flow mechanisms. *Journal of Contaminant Hydrology*, **43**(3-4), 211–238. [dx.doi.org/10.1016/S0169-7722\(00\)00085-1](https://doi.org/10.1016/S0169-7722(00)00085-1).
- [16] MORALES, F. A. (2014) Homogenization of geological fissured systems with curved non-periodic cracks. *Electronic Journal of Differential Equations*, **Vol. 2014 No 189**, 1–21.
- [17] MORALES, F. A. & SHOWALTER, R. (2012) Interface Approximation of Darcy Flow in a Narrow Channel. *Mathematical Methods in the Applied Sciences*, **35**, 182–195.
- [18] PESZYŃSKA M., SHOWALTER R.E. AND YI S.-Y. (2012) Interface Flow and transport when scales are not separated: numerical analysis and simulations of micro- and macro-models. *International Journal of Numerical Analysis and Modeling*, **12**(3), 476–515.
- [19] SHOWALTER, R. (1997) *Microstructure Models of Porous Media*. In Ulrich Hornung editor *Homogenization and Porous Media*, vol. 6 of *Interdisciplinary Applied Mathematics*. Springer-Verlag, New York.

- [20] SHOWALTER, R. E. & WALKINGTON, N. J. (1991) Micro-structure models of diffusion in fissured media. *Journal of Mathematical Analysis and Applications*, **155**, 1–20.
- [21] SPAGNUOLO, A. M. & WRIGHT, S. (2003) Analysis of a multiple-porosity model for a single-phase flow through naturally fractured porous media. *Journal of Applied Mathematics*, **2003:7**, 327–364. dx.doi.org/10.1155/S1110757X03205143.
- [22] SPAGNUOLO, A. M. & WRIGHT, S. (2003) Analysis of a multiple-porosity model for a single-phase flow through naturally fractured porous media. *Journal of Applied Mathematics*, **2003:7**, 327–364. dx.doi.org/10.1155/S1110757X03205143.
- [23] TASSONE A. & SANTOMAURO M. & MNICHETTI M. & CERREDO M. A. & REMESAL M. B. & LIPPATI H. & LODOLO E. & VILAS J.F. (2010) Imaging subsurface lithological and structural features by resistivity tomography: North Beagle Channel (Tierra del Fuego, Argentina), *Revista Mexicana de Ciencias Geológicas*, v. **27(3)**, 562–572.
- [24] WANG, S., FENG, Q. & HAN, X. (2013) A Hybrid Analytical/Numerical Model for the Characterization of Preferential Flow Path with Non-Darcy Flow. *PLoS ONE*, **8(12)**, e83536. doi:10.1371/journal.pone.0083536.
- [25] ZHANG Z. & NEMCIK J. (2013) Friction Factor of Water Flow Through Rough Rock Fractures. *Rock Mech Rock Eng*, **46**, 1125–1134. doi:10.1007/s00603-012-0328-9.